Special Collection

Tin-Containing Graphite for Sodium-Ion Batteries and Hybrid Capacitors

Thangavelu Palaniselvam,[a, b] Binson Babu,[b] Hyein Moon,[c, d] Ivana Hasa,[c, d] Aggunda L. Santhosha,[a] Mustafa Goktas,[a] Ya-Nan Sun,[a, e] Li Zhao,[e] Bao-Hang Han,[e] Stefano Passerini,[c, d] Andrea Balducci,*[b] and Philipp Adelhelm*[a, b]

The limited Na-storage capacity of graphite anodes for sodium-ion batteries (~110 mAh g^{-1}) is significantly enhanced by the incorporation of nanosized Sn (17 wt%). The composite (SntGraphite), prepared by simple annealing of graphite with $SnCl_2$, shows a specific capacity of 223 mAh g^{-1} (at 50 mA g^{-1}) combined with excellent cycle life (i.e., 96% of capacity retention after 2,200 cycles at 1 A g^{-1}) and initial Coulomb efficiency (90%). The combined storage of sodium in graphite (by solvent co-intercalation) and Sn (by alloy formation) is followed by in situ X-ray diffraction and in situ electrochemical dilatometry (ECD). While the additional tin almost doubles the electrode capacity, its contribution to the electrode expansion (~3%) is surprisingly small. The use of SntGraphite as anode for sodium-ion hybrid capacitors with activated carbon as cathode provides a maximum energy and power density of ~93 Wh kg^{-1} and 7.8 kW kg^{-1}, with a capacity retention of ~80% after 8,000 cycles.

1. Introduction

Sodium-ion batteries (SIBs) are increasingly considered as an alternative energy storage technology to lithium ion batteries (LIBs) providing long cycle life, as well as high energy and power density ideally employing abundant elements.[1] Due to the similarity with LIBs, SIBs are considered a drop-in technology with energy densities slightly below LIBs, but significantly above lead-acid batteries. Similarly, sodium-ion hybrid capacitors (SIHCs) aim at bridging the performance gap between SIBs and supercapacitors.[2] In most cases, SIHCs combine a battery anode with a supercapacitor cathode. Therefore, an important challenge faced by SIBs is applicable to SIHCs as well, i.e., finding a suitable anode material that provides high capacities at very high rates over many cycles.

Graphite is the most popular anode for LIBs. An important limitation of SIBs, however, is the thermodynamic instability of sodium-rich, binary graphite intercalation compounds (b-GIC) in carbonate-based electrolytes disabling the use of the graphite anode.[3–4] Earlier studies on sodium storage in graphite reported a maximum specific capacity of about 20–30 mAh g^{-1}.[5] More recently, we demonstrated that graphite can provide specific Na storage capacities around 110 mAh g^{-1} over many cycles and at very high rates, using ethers as electrolyte solvents.[6] For example, a specific capacity of close to 80 mAh g^{-1} is obtained at the current density of 11 A g^{-1} in our previous research.[7] This impressive rate performance is attributed to the co-intercalation of solvent molecules along with Na^+ ions between the graphene layers. This mechanism leads to the formation of thermodynamically stable ternary graphite intercalation compounds (t-GIC).[8] Although the capacity of 110 mAh g^{-1} requires improvement for being attractive as battery electrode, this value is high compared to a supercapacitor electrode. Thanks to the high rate performance exhibited in ether-based electrolytes,[9] graphite remains therefore an interesting anode material for SIBs and SIHCs.[10] Motivated by the advantageous properties of graphite, several studies have been published with the aiming at a better understanding of the reactionmechanism and at sketching out the diversity and applicability of t-GICs electrodes.[11–18] Results on the use of micro-sized graphite for SIHC with ether electrolytes showed a high initial Coulombic efficiency (ICE,

[a] Dr. T. Palaniselvam, A. L. Santhosha, Dr. M. Goktas, Dr. Y.-N. Sun, Prof. Dr. P. Adelhelm
Department of Chemistry
Humboldt-University Berlin
Brook-Taylor Str. 2, 12489 Berlin, Germany
E-mail: philipp.adelhelm@hu-berlin.de
[b] Dr. T. Palaniselvam, Dr. B. Babu, Prof. Dr. A. Balducci, Prof. Dr. P. Adelhelm
Institute of Technical Chemistry and Environmental Chemistry
and Center for Energy and Environmental Chemistry Jena (CEEC Jena)
Friedrich Schiller University Jena
Philosophenweg 7a, 07743 Jena, Germany
E-mail: andrea.balducci@uni-jena.de
[c] H. Moon, Dr. I. Hasa, Prof. Dr. S. Passerini
Helmholtz Institute Ulm (HIU)
Helmholtzstrasse 11, 89081 Ulm, Germany
[d] H. Moon, Dr. I. Hasa, Prof. Dr. S. Passerini
Karlsruhe Institute of Technology (KIT)
P.O. Box 3640, 76021 Karlsruhe, Germany
[e] Dr. Y.-N. Sun, Prof. Dr. L. Zhao, Prof. Dr. B.-H. Han
CAS Key Laboratory of Nanosystem and Hierarchical Fabrication
CAS Center for Excellence in Nanoscience
National Center for Nanoscience and Technology
Beijing 100190, China.

Supporting information for this article is available on the WWW under https://doi.org/10.1002/batt.202000196

Special Collection *An invited contribution to a joint Special Collection between ChemElectroChem and Batteries & Supercaps dedicated to research Beyond Lithium-Ion Batteries*

94%) and long cycle life, for example.[19] The high ICE is a clear advantage over conventionally used anode materials for SIHC, which, often being nanostructured materials, offer ICE values typically between 30%–60% due to excessive electrolyte decomposition along with solid electrolyte interphase (SEI) formation.[20]

As an alternative to graphite, several micro and nanostructured materials have been proposed for SIBs' anodes.[21–22] Based on the Na storage mechanism, these materials can be roughly classified into three types 1) carbon-based materials, sodium titanate (intercalation, insertion/adsorption) 2) metal oxides and sulfides (conversion reaction) 3) high capacity anode materials tin (Sn), Sb, Bi, Si, Ge, and P (alloying /dealloying reaction).[23–24] Carbons, such as hard/soft carbons and graphene-based materials are intensively studied as alternatives to graphite.[25] Graphene or reduced graphene oxide (rGO) anodes deliver specific capacities in the range of 200–250 mAh g^{-1}, though they show a very high initial irreversible capacity loss.[26] Typically, sodium storage in hard carbon is reflected in a sloping region below 1 V vs Na^+/Na and a plateau region below 0.1 V vs Na^+/Na, delivering specific capacities between 75–125 mAh g^{-1} and 200–300 mAh g^{-1}, respectively.[27] The capacity of hard carbon can be increased by tuning the microstructure and the annealing temperature,[28] however, significant capacity improvement is only obtained in the plateau region, which is likely too close to the metal plating potential and hence might not be a viable strategy for practical application.

On the other hand, the metal oxides and sulfides can lead to high capacities, but show poor cycle life with voltages of 1.5 V.[29] As an alternative to both carbon and metal oxides, alloys are gaining attention. Sn is very attractive due to its very high theoretical capacity (847 mAh g^{-1}) combined with a very attractive redox activity range (0.15–0.40 V vs. Na^+/Na).[30–31] However, Sn undergoes large volume expansion during sodiation (420% for the formation of $Sn_{3.75}Na$), leading to poor cycle life. An efficient way to overcome this limitation is making composites of Sn with carbon nanostructures. Our previous study has demonstrated that the combination of graphene nanoplatelets (GnP), nitrogen-doping and Sn (i.e., SnNGnP) in a nanocomposite enables stable cycling (1,000 cycles with 83% of retention capacity) and reduces the volume expansion of the electrode during cycling to values as low as ~14%.[32] However, the relatively high surface area of the material (60 $m^2 g^{-1}$) and the loose structure compromise the volumetric capacity of the electrode (253 mAh cm^{-3}) which is only around half of what is obtained for graphite electrodes in LIBs (approx. 570 mAh cm^{-3} allowing an electrode porosity of ~30%).[33] Careful optimization of electrode composition, loading and packing density is therefore needed for practical application.

Considering the electrolyte, ether-based substitute electrolytes with systems showed good compatibility with various anodes for SIBs including TiO_2,[34–35] Sn,[36] Bi,[37] SnSb,[38] reduced graphene oxide,[39] sodium,[9,40] and so on. Unlike the more common carbonate-based electrolytes, ether-based electrolytes generally show a better reductive stability and lead to a thinner and more stable SEI. Overall, this leads to a higher ICE and faster charge transfer dynamics.

Here, we discuss the synthesis of a graphite-Sn composite material denoted as SntGraphite (17 wt% Sn), which is prepared by annealing of $SnCl_2$ with graphite in inert atmosphere. The material is structurally characterized by TEM and XRD. The Na storage behavior is studied by galvanostatic cycling and cyclic voltammetry. In situ electrochemical dilatometry (ECD) and in situ XRD are used to study the electrode "breathing" and the storage mechanism. The material is further tested as negative electrode in a Na-ion hybrid capacitor device.

2. Results and Discussion

2.1. Synthesis and Characterization of SntGraphite

The synthesis of SntGraphite is sketched in Scheme 1 and described in the experimental section. At first, graphite was mildly oxidized by thermal treatment at 630 °C in air atmosphere. This process is done to facilitate the interaction of graphite with the Sn-precursor. Subsequently, 500 mg of thermally activated graphite (i.e. tGraphite) was dispersed in ethanol solution (200 mL) containing 500 mg of $SnCl_2$ and allowed for mechanical rotation for 12 hours. After evaporation of ethanol, the remaining solid mixture was grounded and annealed at 900 °C in Ar atmosphere. The final composite was termed as SntGraphite. The morphology and structure of SntGraphite were characterized by TEM and XRD analysis.

Figure 1a–d shows TEM images of the graphite particle edges before and after thermal activation. Before activation,

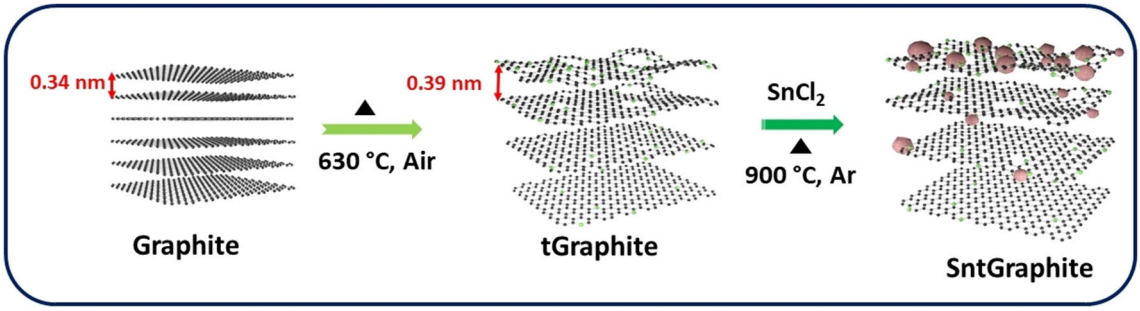

Scheme 1. Synthesis pathway for the preparation of SntGraphite.

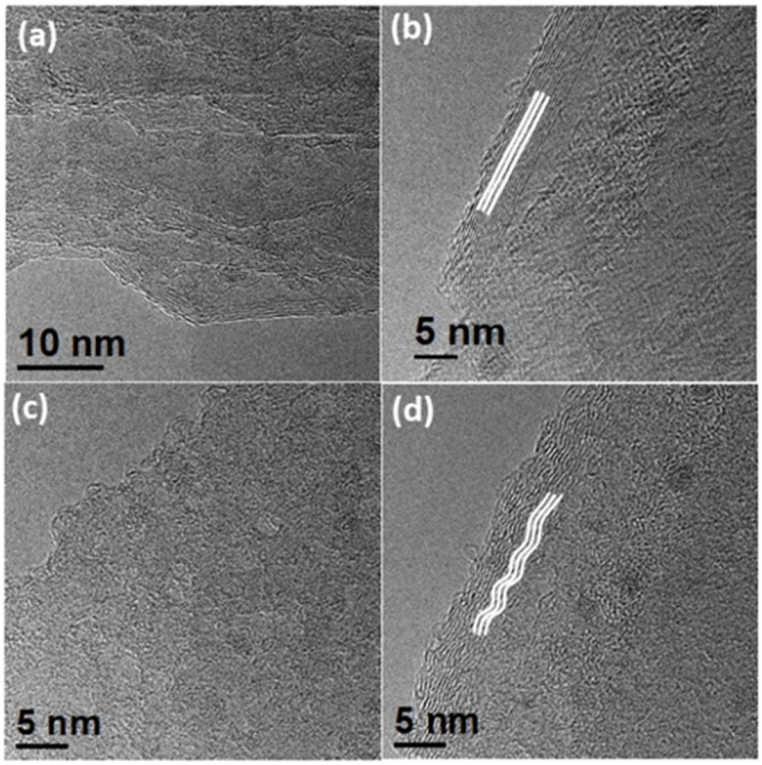

Figure 1. TEM images of a-b) Graphite and c-d) tGraphite.

graphite (Figure 1a-b) shows the expected, well-defined layered structure with average interlayer distances in the range of ~0.34 nm. After activation, the graphene layers in tGraphite appear more wrinkled with turbostratic order and hence with a slightly larger interlayer spacing (~0.39 nm, see Figure 1c–d and Figure S1).

The structure and morphology of SntGraphite were also characterized by TEM (Figure 2). The images show that the Sn particles are nano-sized (3 to 5 nm) and well distributed on the surface of the graphite, with only little agglomeration. The crystallinity of the Sn nanoparticles can be seen from the high-resolution image and the selected area electron diffraction (SAED) image, see insets of Figure 2a and b. The d-spacing of 0.28 nm corresponds to the (200) planes of Sn. The fine dispersion of Sn in the graphite is also seen from STEM-EDS mapping (Figure 2c–e).

XRD patterns of graphite, tGraphite, and SntGraphite are shown in Figure S2. The typical graphite reflections are found in all samples indicating that the major fraction of graphite maintains its graphitic structure during the synthesis. This result means that the turbostratic disorder observed by TEM is more located at the particle surface, i.e. the thermal activation leads to oxidation of the graphite surface. This is in line with N_2 physisorption measurements which show only a moderate increase in Brunauer-Emmett-Teller (BET) surface area for tGraphite (~4 $m^2 g^{-1}$) compared to graphite (~1 $m^2 g^{-1}$), see Figure S3. For SntGraphite, crystalline Sn can be clearly seen from the reflections at 30.8° (200 planes) and 32.1° (101 planes) respectively. The total Sn content in SntGraphite was determined as 17 wt% using TGA analysis (Figure S4) and the BET specific surface area of SntGraphite was ~3 $m^2 g^{-1}$ (Figure S3).

2.2. Na Storage Behavior

The electrochemical properties of SntGraphite were investigated by cyclic voltammetry (CV) and galvanostatic charge-discharge measurements. Figure S5a shows the CV curves of SntGraphite and graphite cycled between 0.005 V to 1.2 V vs Na^+/Na with a scan rate of 0.1 mV s^{-1}. As observed previously, the CV for graphite (Figure S5a) shows the well-resolved cathodic and anodic peaks corresponding to the (de)sodiation in graphite through t-GIC formation.

As compared to graphite, the SntGraphite electrode shows several more peaks i.e. six cathodic peaks at 0.84, 0.72, 0.62, 0.18, 0.11 and 0.01 V vs Na^+/Na. The first three peaks can be correlated with the formation of Na–C phases, while the remaining peaks relate to the formation of Na–Sn intermetallic compounds. In the anodic scan, four peaks at 0.24, 0.54, 0.71 and 0.99 V vs Na^+/Na which are associated with desodiation of Na–Sn and Na–C intermetallic compounds. The asymmetric behavior (different number peaks for sodiation and desodiation) is due to Sn.[32,36] Overall, the CV curves of SntGraphite show that Na storage in SntGraphite occurs by t-GIC and Na–Sn alloy formation. Figure 3a represents the voltage profile for SntGraphite cycled at 50 mA g^{-1} in the voltage window of 0.005 to 1.2 V vs Na^+/Na. For comparison, the voltage profile for tGraphite recorded under identical conditions is shown in

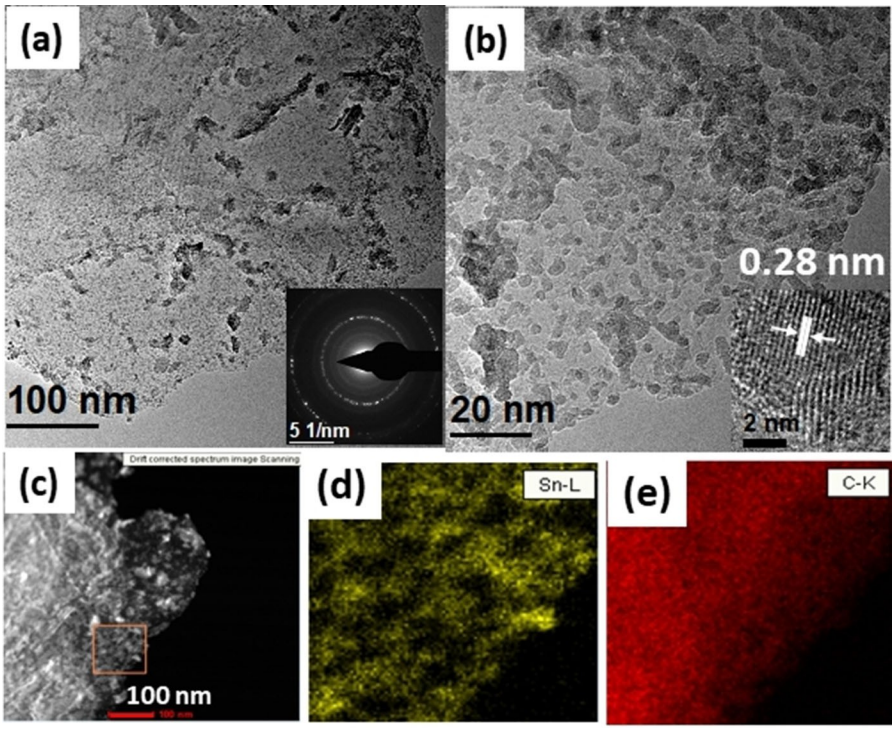

Figure 2. a–b) TEM images of SntGraphite at different magnifications. c) TEM images of SntGraphite in dark mode. d–e) elemental mapping of tin and carbon. Inset of (a) is the SAED pattern of SntGraphite. Inset of (b) is the HRTEM image of SntGraphite.

Figure 3b. Initially, the SntGraphite electrode delivers a specific capacity of around 247 mAh g^{-1} with an initial Coulombic efficiency (ICE) as high as ~90 %. This value is very close to the ICE obtained for pure graphite electrodes (~92 %, Figure S6)[32] and, importantly, much higher compared to other Sn/C-based anodes for which the ICE is typically between 60–75 % (with carbonates electrolytes), see e.g. Ref. [32]. Such high ICE values are an important requirement for application as otherwise too much Na is lost from the counter electrode.

In the next cycle, the specific capacity reduced to 223 mAh g^{-1} and remained constant afterwards. No apparent fading was observed up to 100 cycles, indicating a highly reversible and stable electrode reaction. Considering the specific capacity for tGraphite (115 mAh g^{-1}) (Figure 3b) and Graphite (119 mAh g^{-1}, Figure S6), the obtained capacity for SntGraphite is significantly higher and a direct result of the additional tin (Sn). This can be easily understood from considering the theoretical specific capacities for Sn (847 mAh g^{-1}) and tGraphite (115 mAh g^{-1})[8] and their contents in SntGraphite (17 wt% Sn and 83 wt% tGraphite). Overall, this amounts to a theoretical capacity of 240 mAh g^{-1} for SntGraphite (calculation given in the Supporting Information). The capacity obtained in the second cycle (223 mAh g^{-1}) is very close to this theoretical value, suggesting a high utilization (~93 %, see Supporting Information) of Sn and Graphite for Na storage. The voltage profile shows defined plateaus during sodiation and desodiation, in line with a combined storage over Na–Sn alloys and t-GICs, see Figures 3a, b. The plateaus can be more clearly seen from the dq/dV plot (Figure S5b) which matches well with the CV data (Figure S5a). The formation of t-GIC compounds and Na–Sn intermetallic compounds were confirmed by in situ XRD which is discussed further below.

Furthermore, the rate performance for SntGraphite was studied at different current densities ranging from 0.05 to 2 A g^{-1} (Figure 3c). With increasing current densities, the SntGraphite delivers the capacities of 226, 213, 208, 196, 184 and 134 mAh g^{-1} at 0.05, 0.1, 0.2, 0.5, 1.0, and 2.0 A g^{-1}, respectively. When the current density is down to 0.05 A g^{-1}, the specific capacity recovers to 221 mAh g^{-1} and retains the same value for next the 50 cycles, demonstrating excellent rate performance and stability. Moreover, the active SntGraphite delivers a specific capacity at 40 mAh g^{-1} even at 20 A g^{-1} (Figure S7) showing the ability to store Na even at high currents. The long-term cycling of SntGraphite was studied over 2,200 cycles at 1 A g^{-1} (Figure 3d). Starting from 170 mAh g^{-1} (second cycle) the reversible capacity remains at 164 mAh g^{-1} after 2,200 cycles corresponding to a retention of 96 %. Postmortem studies on the SntGraphite electrode (after 500 cycles) by TEM (see Figure S8) show no apparent changes of the morphology of Sn indicating that diglyme is compatible for both graphite and Sn. At a mass loading of 7.9 mg cm^{-2}, the active composite delivers a reversible capacity of 220 mAh g^{-1} corresponding to the areal specific capacity of ~1.5 mAh cm^{-2} (Figure S9). This is still at the lower end compared to commercialized LIB anodes (1–3 mAh cm^{-2}) but quite reasonable considering the first-time use of the material. We also tried higher loadings but buckling of the electrodes occurred for loadings $\geq$ 7 mg cm^{-2}. Higher loadings are certainly possible but will require technical optimization which is outside the

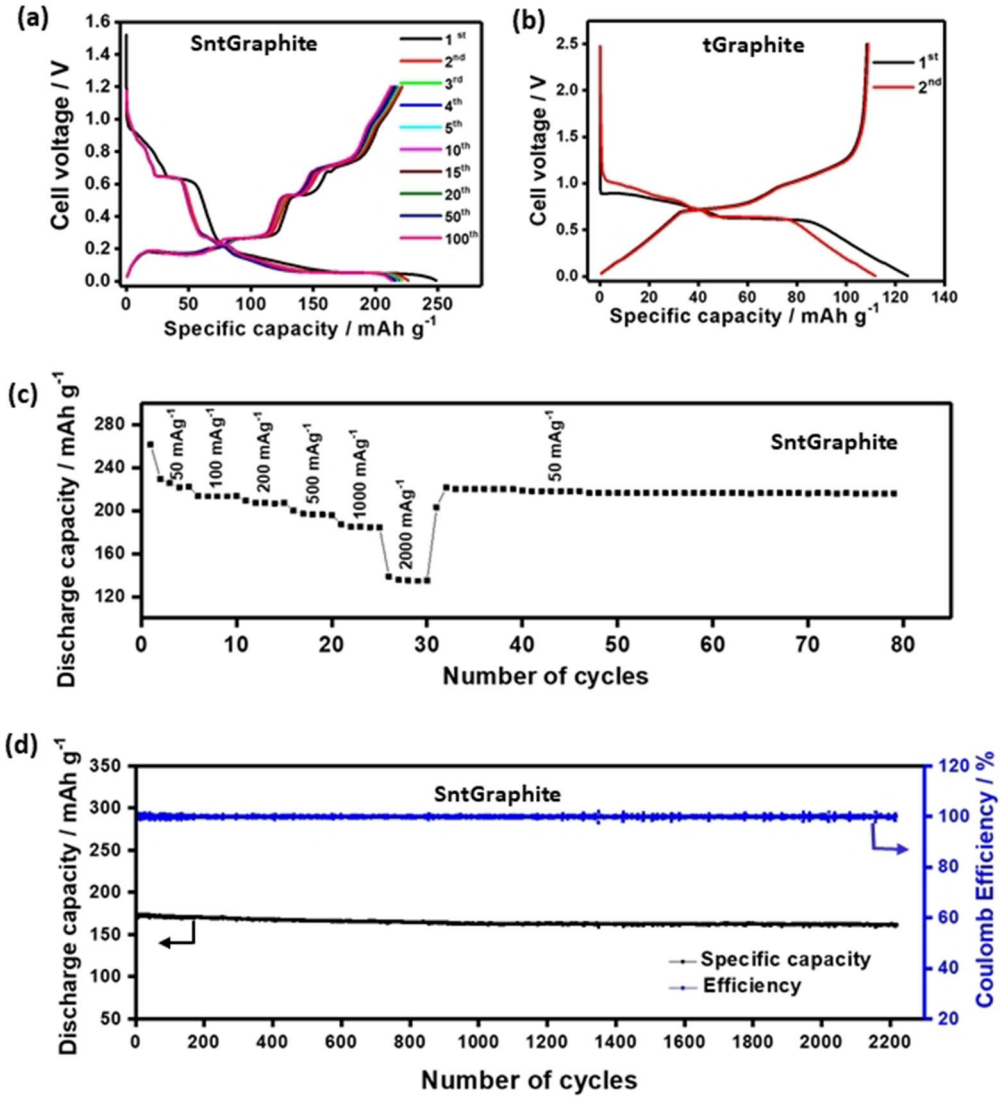

Figure 3. Charge-discharge curves of a) SntGraphite and b) tGraphite, measured at 50 mAg^{-1}. c) Rate capability of SntGraphite electrode measured from 50–2000 $mA\,g^{-1}$. d) Cycling stability of SntGraphite electrode evaluated with charge/discharge rates of 1 $A\,g^{-1}$ for 2,200 cycles. Measurements performed in two-electrode geometry with sodium as counter electrode. Capacity values refer to the weight of SntGraphite.

scope of this study. Overall, the addition of Sn (17 wt%) to graphite leads to a significant increase in capacity without impairing the advantages of long cycle life and high ICE.

2.3. In Situ Electrochemical Dilatometry (ECD) and In Situ XRD

Sodiation of bulk Sn and graphite leads to large volume changes which is a key limitation for their use in practical cells. We therefore studied the electrode expansion using in situ electrochemical dilatometry (ECD). Results for graphite and SntGraphite are compared in Figure 4. The behavior for graphite is well in line with our previous findings,[8] i.e. the electrode thickness becomes larger during the first cycle followed by a fairly constant "breathing" upon further cycling. The breathing in the range of 198.6–136.4 µm (68%) is the result of the solvent co-intercalation leading to a much larger interlayer spacing compared to graphite. For SntGraphite, the additional Na storage in Sn leads to a more pointed dilatometer signal upon cycling. This shows that the additional storage mechanism has a direct consequence on the electrode "breathing". This is more clearly seen from Figure 5 which shows a close-up of the 1st cycle for Graphite and SntGraphite.

For graphite, the potential profile shows three different regions (A from 1.0 V to 0.7 V, B at a plateau of 0.7 V and C from 0.7 V to 0.005 V). These regions can be also distinguished in the dilatometer signal (see Ref. [8] for a discussion). For SntGraphite, the combined storage behavior of graphite and Sn can be again well seen from the potential profile. Sodiation of Sn starts at potentials below 0.2 V which is indicated by region D. The interesting point is that while region D roughly doubles the electrode capacity, the increase in electrode thickness is negligible (from 118% total increase, only around 3% are due

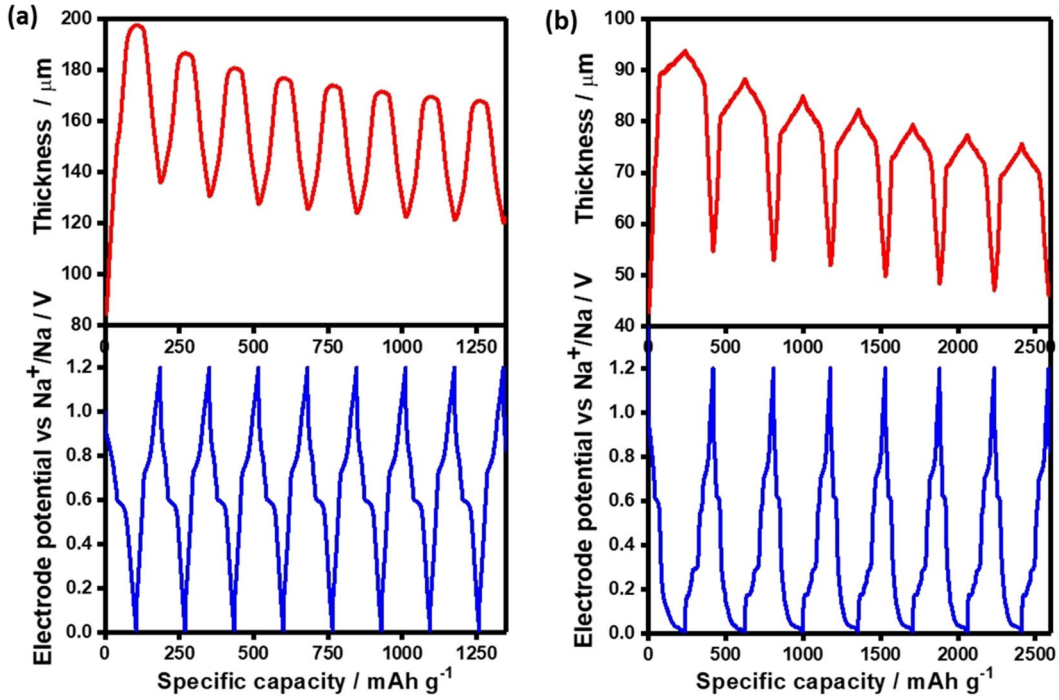

Figure 4. In situ electrochemical dilatometry measurements for a) Graphite and b) SntGraphite (measured at 30 mA g^{-1}). The x-axis shows the cumulative capacity over seven consecutive cycles. Measurements were done in three-electrode geometry with sodium as counter and reference electrode.

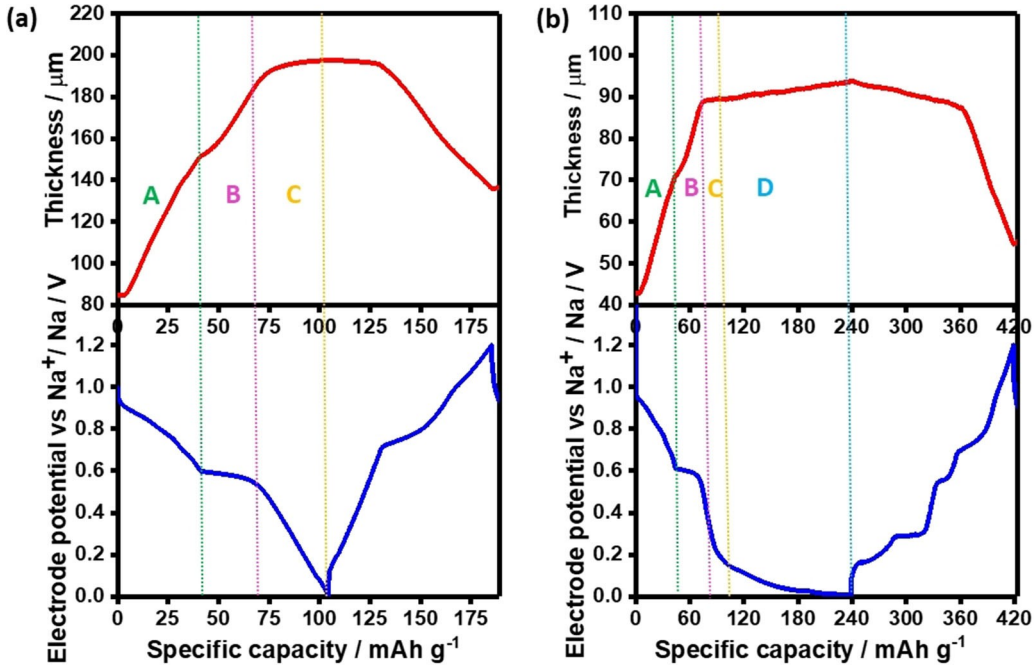

Figure 5. The thickness changes and corresponding potential profile for a) Graphite and b) SntGraphite obtained during in situ electrochemical dilatometry measurements (first cycle). The applied current density was 30 mA g^{-1}. Measurements performed in three-electrode geometry with sodium as counter and reference electrode.

to alloy formation). This means that storing Na in Sn leads to a much smaller electrode breathing compared to storing the same amount of (solvated) Na in graphite. This appears surprising, giving the fact that the theoretical volume expansion for Sn (420%)[41] is about twice as large compared to graphite (240–250%).[42] The behavior is likely due to the fine dispersion of Sn in the graphite which predominantly leads to an expansion within electrode, i.e. into the electrode porosity. This finding can well explain the good cycle life obtained for this material, see Figure 3d.

Further evidence for the combined storage of Na in graphite and Sn was obtained by in situ XRD. Potential profiles and corresponding XRD patterns of the SntGraphite electrode for the 1st cycle are shown in Figure 6. Although only partial recharge was possible in the in situ cell, the discharge curve matches well with the ones obtained in coin cells set up. During sodiation, the graphite reflections show the expected change related to a staged t-GIC formation[43–44] At OCV condition (Figure 6b), the SntGraphite electrode showed a sharp reflection at 26.4° corresponding to (002) plane of graphite and a pair of reflexes at 30.6° and 32.0° corresponding to the (200) and (101) planes of Sn. Once the sodiation commences (from OCV to 0.6 V *vs* Na^+/Na, at scan number 0), the (002) reflection of graphite splits into two new reflections at $2\theta = 24.5°$ (005) and 28.6° (006) indicating the formation of several high stage t-GICs.

The reflections gradually separate from each other until 0.5 V, where the positions are maintained and the transition of stage II into stage I takes place. No further apparent changes related to the t-GIC take place when further decreasing the voltage to 0.005 V. At around 0.3 V, the Sn reflections start to disappear and some new reflections corresponding to the Na–Sn intermetallic compounds starts to appear (Figure S10). The reaction is reversed during de-sodiation. Firstly, the reflections of the Na–Sn intermetallic compounds disappear along with the reappearance of Sn. Secondly, the t-GIC reflections start to disappear (as mentioned, charging was not fully completed). Overall, the combined storage mechanism of sodium in graphite and Sn could be clearly followed by in situ XRD.

2.4. Use of SntGraphite in a Hybrid Sodium-Ion Capacitor

In order to understand the effectiveness of SntGraphite as anode for hybrid Na-ion capacitor, a quantitative kinetic analysis was conducted.[45] To investigate the kinetics of charge storage in Sn-Graphite composite electrode, the cyclic voltammograms (CV) are recorded at different scan rates from 0.1–5.0 mV s^{-1} (Figure S11). The total charge stored in CV is a combination of bulk diffusion controlled faradaic contributions from Na ions intercalation as well as alloying process and the surface-controlled contributions, which is a combination of redox pseudocapacitance and the non-faradaic contribution from the double layer formation. The "surface" controlled and "bulk" diffusion-limited charge storage process in this material can be distinguished from the power law relation:[46] The current at each potential $i(V)$ can be represented as [Eq. (1)],

$$i(V) = k_1 v + k_2 v^{1/2} \quad (1)$$

where $k_1 v$ and $k_2 v^{1/2}$ are the current contributions due to the surface and bulk diffusion-controlled processes, respectively, and 'v' is the scan rate, V is the potential, k_1 and k_2 are coefficient of "surface" and "bulk" processes, respectively. Note, however, that results of this equation should be only taken as a very rough indicator to separate both types of processes as the simplicity of the equation does not reflect the complex structure of the electrode (hence the notation for "surface" and "bulk" in quotation marks).[47] Figure S12 shows the cyclic voltammogram at different scan rates clearly differentiating the contribution of current from "surface" controlled process (shaded region) from the "bulk" diffusion-limited process. For instance, the analysis shows that at a scan rate of 2.0 mV s^{-1}, about 60% of the total charge stored in SntGraphite composite is the "surface" controlled process (shaded area). The histogram

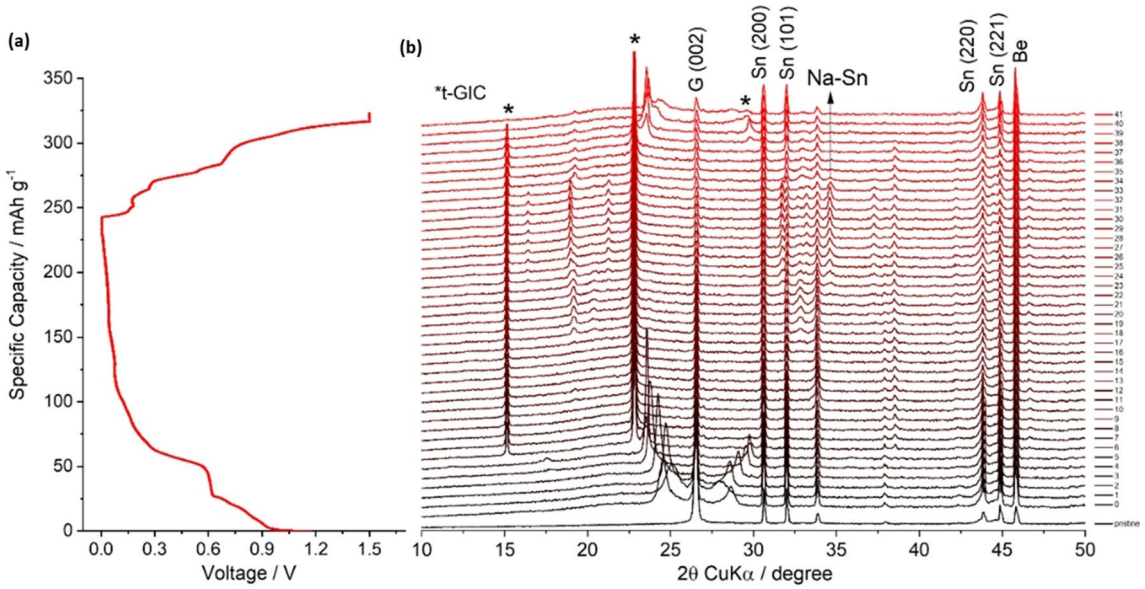

Figure 6. In situ XRD measurement: a) Voltage profile vs. specific capacity of SntGraphite in diglyme electrolyte (1st cycle, 30 mA g^{-1}), b) Corresponding XRD patterns. Measurements performed in two-electrode geometry with sodium as counter electrode.

in Figure 7 summarizes the diffusion controlled and non-diffusion ("surface") controlled contribution of the SntGraphite composite at different scan rates. The results indicate that the fraction of the "surface storage" increases as the scan rate increases and reaches a contribution of ~78.4% at a high scan rate of 5 mV s^{-1}.

In order to check the performance of SntGraphite in high power applications, we fabricate a sodium-ion capacitor with SntGraphite as the negative electrode and activated carbon (AC) as the positive electrode. Before fabricating the full cell hybrid ion capacitor, it is important to pre-sodiate the SntGraphite. For this, SntGraphite was individually cycled in the potential range of 0–1.2 V vs Na^+/Na. On the other side, the AC was cycled in the potential range of 3.0–4.0 V vs Na^+/Na (Figure S13). The hybrid cell was fabricated by combining the pre-sodiated SntGraphite with an AC (details about the cell are available is Figure 8a). Figure 8b shows the galvanostatic charge discharge curve of SntGraphite//AC Na-ion capacitor at different current densities. The linear behavior of the voltage vs time indicates the prominent capacitive behavior of the full cell hybrid ion capacitor.

During charging process, the Na ions are inserted into the negative electrode, while the anions PF_6^- adsorbed at the surface of the AC. A reverse process is taking place during the discharge. Figure 8c shows the rate capability performance of SntGraphite//AC. It can be observed that the cell displays a capacity of 50 mAhg^{-1} at 0.25 Ag^{-1}, while it exhibits a capacity of 22 mAh g^{-1} at 5.0 A g^{-1}. The system is also showing excellent rate performance. Figure S14 shows the galvanostatic charge-discharge of the full cell as well as anode and cathode vs. Na^+/Na at a current density of 0.25 A g^{-1} before and after the rate capability study.

The energy and the power densities of the investigated SntGraphite//AC sodium-ion capacitor have also been estimated. The device exhibits a maximum energy density of ~93 Wh kg^{-1} at a power density of 495 W kg^{-1} and provides an energy density of 33 Wh kg^{-1} at a high-power density of 7.8k W kg^{-1}. These values are comparable or even higher than those reported for other Na-ion capacitors (Figure S15). Finally, the cyclic stability of the device has also been investigated. As shown in Figure. 8d and Figure S16, the investigated device shows an excellent cycling stability and high coulomb efficiency (close to 100%) over 8000 cycles carried out at a current density of 1 A g^{-1}. Considering these results, the SntGraphite based electrode investigated in this work appears as an interesting candidate also for the realization of high-power devices.

3. Conclusions

A SntGraphite composite containing 17 wt% Sn was synthesized by simple annealing of $SnCl_2$ with thermally modified graphite. The resulting composite with a BET surface area of around 3 $m^2 g^{-1}$ delivered a very high ICE (~90%) in the first cycle and provided a Na storage capacity of 223 mAh g^{-1} at 50 mA g^{-1}, i.e. the capacity compared to graphite (110 mAh g^{-1}) is roughly doubled. The electrode also showed a very high cycling stability maintaining 96% of its initial capacity after 2200 cycles at 1 A g^{-1}. Electrochemical measurements, in situ ECD and in situ XRD showed that the sodium storage in SntGraphite occurs through a combined storage mechanism based on t-GIC formation and Na–Sn alloy formation. Interestingly, while the addition of Sn roughly doubles the electrode capacity, its contribution to the electrode breathing is negligible. From an expansion of 118% (1st cycle), only 3% is due to Sn, most likely due to the good dispersion of Sn nanoparticles in the graphite matrix. Furthermore, the kinetic studies show the suitability of SntGraphite as negative electrode for SIHCs. The fabricated SIHC showed a maximum energy density of ~93 Wh kg^{-1} at a power density of 495 W kg^{-1} and an energy density of 33 Wh kg^{-1} at a power density as high as 7.8 W kg^{-1}

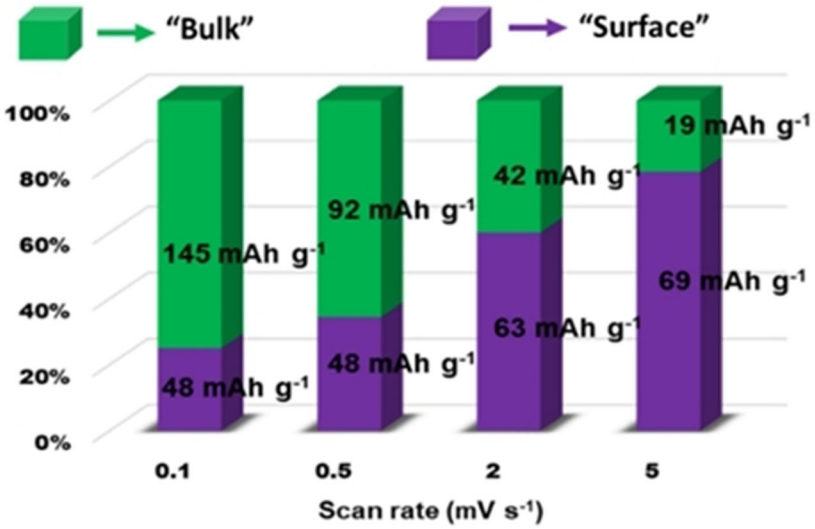

Figure 7. Histogram shows the percentage contribution of "surface" and "bulk" charge storage capacity at different scan rates.

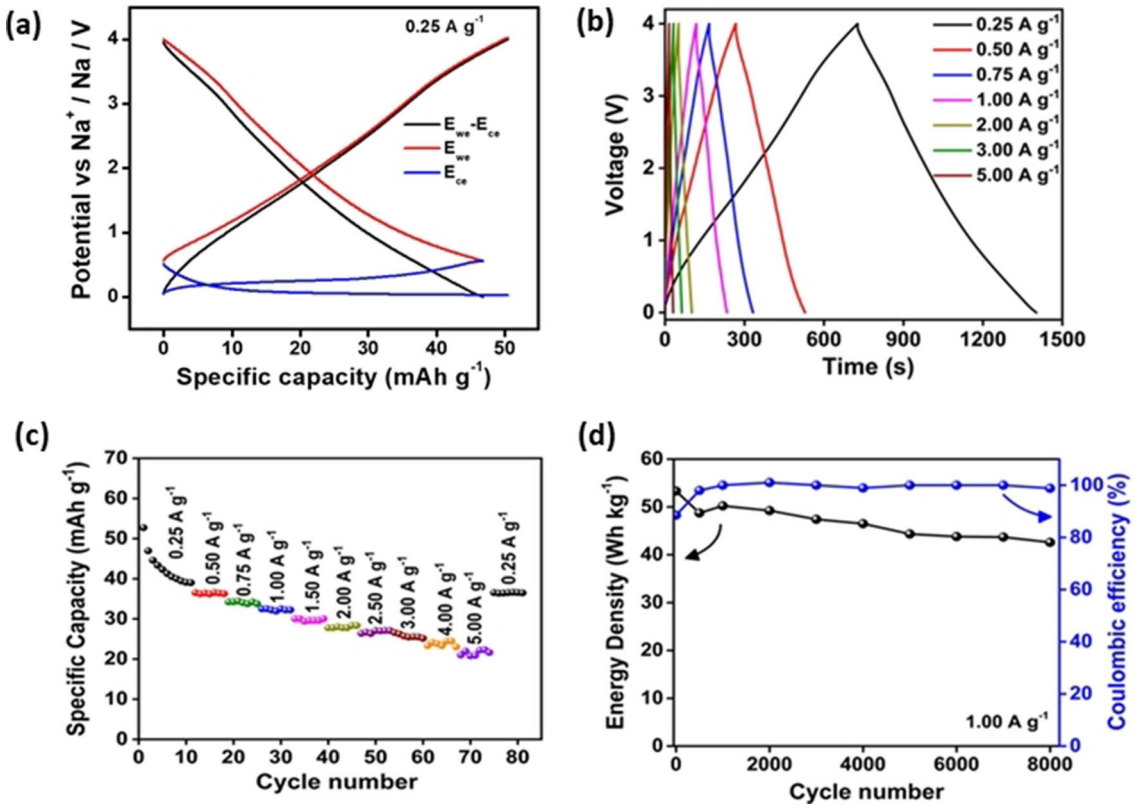

Figure 8. a) Charge-discharge curve of SntGraphite//AC hybrid cell (black curve) cycled at 0.25 A g^{-1} in a three-electrode cell with sodium metal as reference electrode. (The blue curve representing the charge-discharge curve of SntGraphite and the red curve representing the charge-discharge curve of AC). b) Galvanostatic charge-discharge curve of SntGraphite//AC Na-ion capacitor cycled in a potential range of 0–4 V at different current densities, c) rate capability plot of SntGraphite//AC Na-ion capacitors and d) cycling performance as well as Coulombic efficiency of SntGraphite//AC Na-ion capacitor at 1.0 A g^{-1}.

and also exhibits an excellent stability with a capacity retention of about 80% after 8,000 cycles.

Acknowledgements

P.A., T.P., A.B. and B.B. thank the Thüringer Ministerium für Wirtschaft, Wissenschaft und Digitale Gesellschaft (TMWWDG) and the Thüringer Aufbaubank (TAB) for financial support within the project LiNaKon (2018 FGR 0092). P.A., T.P., S.P., I.H., M.H. acknowledge support from the project TRANSITION (03XP0186) funded by the Bundesministerium für Bildung und Forschung (BMBF). P.A., L.Z., Y.S. acknowledge support from the Sino-German Center (GZ1288). M.H., I.H. and S.P. acknowledge the basic funding from the Helmholtz Gemeinschaft. Open access funding enabled and organized by Projekt DEAL.

Conflict of Interest

The authors declare no conflict of interest.

Keywords: sodium-ion battery, anode, graphite, tin, hybrid capacitor

[1] a) P. K. Nayak, L. Yang, W. Brehm, P. Adelhelm, *Angew. Chem. Int. Ed.* **2018**, *57*, 102-120; b) C. Vaalma, D. Buchholz, M. Weil, S. Passerini, *Nat. Rev. Mater.* **2018**, *3*,18013; c) N. Yabuuchi, K. Kubota, M. Dahbi, S. Komaba, *Chem. Rev.* **2014**, *114*, 11636–11682; d) M. H. Han, E. Gonzalo, G. Singh, T. Rojo, *Energy Environ. Sci.* **2015**, *8*, 81–102.
[2] a) J. Ding, W. Hu, E. Paek, D. Mitlin, *Chem. Rev.* **2018**, *118*, 6457–6498; b) H. Wang, C. Zhu, D. Chao, Q. Yan, H. J. Fan, *Adv. Mater.* **2017**, *29*, 1702093; c) S. Dong, L. Shen, H. Li, P. Nie, Y. Zhu, Q. Sheng, X. J. Zhang, *J. Mater. Chem. A* **2015**, *3*, 21277–21283.
[3] a) O. Lenchuk, P. Adelhelm, D. Mollenhauer, *Phys. Chem. Chem. Phys.* **2019**, *21*, 19378–19390; b) Y. Li, Y. Lu, P. Adelhelm, M. M. Titirici, Y. S. Hu, *Chem. Soc. Rev.* **2019**, *48*, 4655–4687; c) H. Moriwake, A. Kuwabara, C. A. J. Fisher, Y. Ikuhara, *RSC Adv.* **2017**, *7*, 36550–36554; d) Y. Liu, B. V. Merinov, W. A. Goddard III, *Proc. Mont. Acad. Sci.* **2016**, *113*, 3735–3739.
[4] M. Winter, J. O. Besenhard, M. E. Spahr, P. Novak, *Adv. Mater.* **1998**, *10*, 725–763.
[5] E. Irisarri, A. Ponrouch, M. R. Palacin, *J. Electrochem. Soc.* **2015**, *162*, 2476–2482.
[6] B. Jache, P. Adelhelm, *Angew. Chem. Int. Ed.* **2014**, *53*, 10169–10173; *Angew. Chem.* **2014**, *126*, 10333–10337.
[7] M. Goktas, B. Akduman, P. Huang, A. Balducci, P. Adelhelm, *J. Phys. Chem. C* **2018**, *122*, 26816–26824.
[8] M. Goktas, C. Bolli, E. J. Berg, P. Novák, K. Pollok, F. Langenhorst, M. v. Roeder, O. Lenchuk, D. Mollenhauer, P. Adelhelm, *Adv. Energy Mater.* **2018**, *8*, 1702724.
[9] M. Goktas, C. Bolli, J. Buchheim, E. J. Berg, P. Novak, F. Bonilla, T. Rojo, S. Komaba, K. Kubota, P. Adelhelm, *ACS Appl. Mater. Interfaces* **2019**, *11*, 32844–32855.
[10] P. Han, X. Han, J. Yao, L. Zhang, X. Cao, C. Huang, G. Cui, *J. Power Sources* **2015**, *297*, 457–463.
[11] B. Jache, J. O. Binder, T. Abeb, P. Adelhelm, *Phys. Chem. Chem. Phys.* **2016**, *18*, 14299–14316.
[12] Z. Zhu, F. Cheng, Z. Hu, Z. Niu, J. Chen, *J. Power Sources* **2015**, *293*, 626–634.

[13] a) G. Yoon, H. Kim, I. Park, K. Kang, *Adv. Energy Mater.* **2017**, *7*, 1601519–1601528; b) Z. L. Xu, G. Yoon, K. Y. Park, H. Park, O. Tamwattana, S. J. Kim, W. M. Seong, K. Kang, *Nat. Commun.* **2019**, *10*, 2598.
[14] H. Kim, J. Hong, G. Yoon, H. Kim, K. Y. Park, M. S. Park, W. S. Yoon, K. Kang, *Energy Environ. Sci.* **2015**, *8*, 2963–2969.
[15] I. Hasa, X. Dou, D. Buchholz, Y. S. Horn, J. Hassoun, S. Passerini, B. Scrosati, *J. Power Sources* **2016**, *310*, 26–31.
[16] A. P. Cohn, K. Share, R. Carter, L. Oakes, C. L. Pint, *Nano Lett.* **2016**, *16*, 543–548.
[17] L. Seidl, N. Bucher, E. Chu, S. Hartung, S. Martens, O. Schneider, U. Stimming, *Energy Environ. Sci.* **2017**, *10*, 1631–1642.
[18] K. Gotoh, H. Maruyama, T Miyatou, M. Mizuno, K. Urita, H. Ishida, *J. Phys. Chem. C* **2016**, *120*, 28152–28156.
[19] X. Liu, G. A. Elia, B. Qin, H. Zhang, P. Ruschhaupt, S. Fang, A. Varzi, S. Passerini, *ACS Energy Lett.* **2019**, *4*, 2675–2682.
[20] a) Y. Li, H. Wang, L. Wang, Z. Mao, R. Wang, B. He, Y. Gong, X. Hu, *Small* **2019**, *15*, 1804539; b) D. Qiu, A. Gao, Z. Xie, L. Zheng, C. Kang, Y. Li, N. Guo, M. Li, F. Wang, R. Yang, *ACS Appl. Mater. Interfaces* **2018**, *10*, 44483–44493; c) S. Li, J. Chen, X. Gong, J. Wang, P. S. Lee, *Small* **2018**, *14*, 1804035.
[21] F. Li, Z. Zhou, *Small* **2018**, *14*, 1702961.
[22] W. Wang, W. Li, S. Wang, Z. Miao, H. K. Liu, S. Chou, *J. Mater. Chem. A* **2018**, *6*, 6183–6205.
[23] X. Yang, A. L. Rogach, *Adv. Energy Mater.* **2020**, *2000288*.
[24] H. Kang, Y. Liu, K. Cao, Y. Zhao, L. Jiao, Y. Wang, H. Yuan, *J. Mater. Chem. A* **2015**, *3*, 17899–17913.
[25] a) K. Wang, Y. Jin, S. Sun, Y. Huang, J. Peng, J. Luo, Q. Zhang, Y. Qiu, C. Fang, J. Han, *ACS Omega.* **2017**, *2*, 687–1695; b) V. Simone, A. Boulineau, A. de Geyer, D. Rouchon, L. Simonin, S. Martinet, *J. Energy Chem.* **2016**, *25*, 761–768.
[26] S. Wu, R. Ge, M. Lu, R. Xu, Z. Zhang, *Nano Energy* **2015**, *15*, 379–405.
[27] A. Kamiyama, K. Kubota, T. Nakano, S. Fujimura, S. Shiraishi, H. Tsukada, S. Komaba, *ACS Appl. Energy Mater.* **2020**, *3*, 135–140.
[28] a) X. Dou, I. Hasa, D. Saurel, C. Vaalma, L. Wu, D. Buchholz, D. Bresser, S. Komaba, S. Passerini, *Mater. Today* **2019**, *23*, 87–104; b) A. G. Martin, J. M. Fernandez, M. Ruttert, M. Winter, T. Placke, J. R. Rico, *Chem. Mater.* **2019**, *31*, 7288–7299; c) Q. Meng, Y. Lu, F. Ding, Q. Zhang, L. Chen, Y.-S. Hu, *ACS Energy Lett.* **2019**, *4*, 2608–2612.
[29] a) S. Yuan, X. Huang, D. Ma, H. Wang, F. Meng, X. Zhang, *Adv. Mater.* **2014**, *26*, 2273–2284; b) T. Zhou, W. K. Pang, C. Zhang, J. Yang, Z. Chen, H. K. Liu, Z. Guo, *ACS Nano* **2014**, *8*, 8323–8333; c) L. David, R. Bhandavat, G. Singh, *ACS Nano* **2014**, *8*, 1759–1770; d) A. Darwiche, C. Marino, M. T. Sougrati, B. Fraisse, L. Stievano, L. Monconduit, *J. Am. Chem. Soc.* **2012**, *134*, 20805–20811.
[30] B. Zhang, G. Rousse, D. Foix, R. Dugas, D. A. D. Corte, J. M. Tarascon, *Adv. Mater.* **2016**, *28*, 9824–9830.
[31] L. D. Ellis, T. D. Hatchard, M. N. Obrovac, *J. Electrochem. Soc.* **2012**, *159*, 1801–1805.
[32] T. Palaniselvam, M. Goktas, B. Anothumakkool, Y. N. Sun, R. Schmuch, L. Zhao, B. H. Han, M. Winter, P. Adelhelm, *Adv. Funct. Mater.* **2019**, *29*, 1900790.
[33] S. Chae, S. H. Choi, N. Kim, J. Sung, J. Cho, *Angew. Chem. Int. Ed.* **2020**, *59*, 110–135.
[34] S. K. Das, B. Jache, H. Lahon, C. L. Bender, J. Janek, P. Adelhelm, *Chem. Commun.* **2016**, *52*,1428–1431.
[35] K. Li, J. Zhang, D. Lin, D. W. Wang, B. Li, W. Lv, S. Sun, Y. B. He, F. Kang, Q. H. Yang, L. Zhou, T. Y. Zhang, *Nat. Commun.* **2019**, *10*, 2598.
[36] J. Huang, X. Guo, X. Du, X. Lin, J. Q. Huang, H. Tan, Y. Zhu, B. Zhang, *Energy Environ. Sci.* **2019**, *12*, 1550–1557.
[37] J. Chen, X. Fan, X. Ji, T. Gao, S. Hou, X. Zhou, L. Wang, F. Wang, C. Yang, L. Chen, C. Wang, *Energy Environ. Sci.* **2018**, *11*, 1218–1225.
[38] W. Brehm, J. R. Buchheim, P. Adelhelm, *Energy Technol.* **2019**, *7*, 1900389.
[39] J. Zhang, D. W. Wang, W. Lv, S. Zhang, Q. Liang, D. Zheng, F. Kang, Q. H. Yang, *Energy Environ. Sci.* **2017**, *10*, 370–376.
[40] K. Westman, R. Dugas, P. Jankowski, W. Wieczorek, Gachot, M. Morcrette, E. Irisarri, A. Ponrouch, M. R. Palacín, J. M. Tarascon, P. Johansson, *ACS Appl. Energy Mater.* **2018**, *1*, 2671–2680.
[41] J. W. Wang, X. H. Liu, S. X. Mao, J. Y. Huang, *Nano Lett.* **2012**, *12*, 5897–5902.
[42] a) B. Jache, J. O. Binder, T. Abe, P. Adelhelm, *Phys. Chem. Chem. Phys.* **2016**, *18*, 14299–14316; b) H. Kim, J. Hong, G. Yoon, H. Kim, K. Y. Park, M. S. Park, W. S. Yoon, K. Kang, *Energy Environ. Sci.* **2015**, *8*, 2963–2969; c) S. C. Jung, Y. J. Kang, Y. K. Han, *Nano Energy* **2017**, *34*, 456–462; d) L. Seidl, N. Bucher, E. Chu, S. Hartung, S. Martens, O. Schneider, U. Stimming, *Energy Environ. Sci.* **2017**, *10*, 1631–1642.
[43] G. Schmuelling, T. Placke, R. Kloepsch, O. Fromm, H. W. Meyer, S. Passerini, M. Winter , *J. Power Sources* **2013**, *239*, 563–571.
[44] a) H. Kim, J. Hong, G. Yoon, H. Kim, K. Y. Park, M. S. Park, W. S. Yoon, K. Kang, *Energy Environ. Sci.* **2015**, *8*, 2963–2969; b) Z. Zhu, F. Cheng, Z. Hu, Z. Niu, J. Chen, *J. Power Sources* **2015**, *293*, 626–634.
[45] V. Augustyn, J. Come, M. A. Lowe, J. W. Kim, P. L. Taberna, S. H. Tolbert, H. D. Abruña, P. Simon, B. Dunn, *Nat. Mater.* **2013**, *12*, 518–522.
[46] M. Sathiya, A. S. Prakash, K. Ramesha, J. M. Tarascon, A. K. Shukla, *J. Am. Chem. Soc.* **2011**, *133*, 16291–16299.
[47] M. Opitz, J. Yue, J. Wallauer, B. Smarsly, B. Roling, *Electrochim. Acta* **2015**, *168*, 125–132.

Manuscript received: August 21, 2020
Revised manuscript received: September 9, 2020
Accepted manuscript online: September 10, 2020
Version of record online: September 30, 2020